INTERNATIONAL JOURNAL FOR NUMERICAL METHODS IN FLUIDS
Int. J. Numer. Meth. Fluids 2008; **1**:1 *Prepared using* fldauth.cls *[Version: 2002/09/18 v1.01]*

Practical evaluation of five partly-discontinuous finite element pairs for the non-conservative shallow water equations

Richard Comblen[1,*], Jonathan Lambrechts[1], Jean-François Remacle[1], Vincent Legat[1]

[1] *Centre for Systems Engineering and Applied Mechanics, Université catholique de Louvain, 4 Avenue Georges Lemaître, B-1348 Louvain-la-Neuve, Belgium*

SUMMARY

This paper provides a comparison of five finite element pairs for the shallow water equations. We consider continuous, discontinuous and partially discontinuous finite element formulations that are supposed to provide second order spatial accuracy. All of them rely on the same weak formulation, using Riemann solver to evaluate interface integrals. We define several asymptotic limit cases of the shallow water equations within their space of parameters. The idea is to develop a comparison of these numerical schemes in several relevant regimes of the subcritical shallow water flow. Finally, a new pair, using non-conforming linear elements for both velocities and elevation (P_1^{NC}-P_1^{NC}), is presented, giving optimal rates of convergence in all test cases. P_1^{NC}-P_1 and P_1^{DG}-P_1 mixed formulations lacks of convergence for inviscid flows. P_1^{DG}-P_2 pair is more expensive but provides accurate results for all benchmarks. P_1^{DG}-P_1^{DG} provides an efficient option, except for inviscid Coriolis-dominated flows, where a small lack of convergence is observed.

KEY WORDS: finite element, shallow water equations, discontinuous Galerkin, non-conforming element, Riemann solver, convergence

1. Introduction

The shallow water equations are a classical model used in a wide area of physics and engineering. They govern flows in estuaries, enable modeling of dam-breaks, floods and tides, and are a key building block for ocean modeling as well as atmosphere modeling. Different numerical methods have been designed for the shallow water equations. Finite volumes are very popular for small scale applications as well as atmosphere modeling, whereas ocean models are mainly based on finite difference methods [1], as described for instance in the book [2]. In the finite element framework, major contributions have been developed with both discontinuous and continuous elements.

The Discontinuous Galerkin (DG) method focuses growing interest since the late nineties, and gives accurate results for hyperbolic conservation laws. Basically, it consists in a volume

*Correspondence to: richard.comblen@uclouvain.be – Tel.: +32 10 47 23 57 – fax: +32 10 47 21 80.

term built as in all finite element methods, and an interface term built as in finite volume methods. High order shape functions can be easily incorporated and at the interfaces, an efficient upwind flux calculation can be performed to tackle the treatment of wave phenomena. Thanks to the absence of continuity constrain on the inter-element boundaries, h-adaptivity [3, 4] and p-adaptivity [5] can be easily implemented. Efficient slope and flux limiters enable positive and shock-capturing versions of the scheme [6, 7, 8]. For atmosphere modeling, the high order capabilities of this scheme are really attractive [9, 10], and the increasing use of DG follows the trend to replace spectral transform methods with local ones. Coastal modeling also benefits from this method [11, 12, 13], and high Froude number flows are accurately captured by this kind of schemes [14, 8]. However, the implementation of elliptic dissipative terms requires some specific modifications, as reviewed in [15]. The local-DG method (LDG) and the interior penalty method (IP) are among the most popular solutions. LDG introduces a mixed formulation for velocities and stress and can be difficult to handle with an implicit time-stepping [16], while IP requires the introduction of an ad-hoc penalty parameter that worsen the conditioning of the discrete spatial operator [17].

Continuous linear finite elements are compelling as they provide high geometric flexibility, they are supposed to be much more accurate than first order methods, and have less degrees of freedom than linear discontinuous Galerkin methods. Further, they naturally handle elliptic operators used as subgrid scale models. Several choices can be made between stable mixed methods, and stabilized methods. Stabilized methods were first designed for scalar advection-diffusion equation, where standard Galerkin method gives oscillating result when mesh Peclet number is too large [18]. For shallow water models, [19, 20, 21, 22] use a symmetric formulation that is stabilized with Petrov-Galerkin approach.

In this paper, we do not analyze stabilized continuous finite elements methods, as it appears to be a really different way to tackle the problem. Furthermore, to develop a fair comparison with all stabilized continuous formulations, it would require a very systematic analysis that is not the topic of this paper.

The search for an efficient mixed formulation for the shallow water equations without explicit stabilization is described in a series of papers [23, 24, 25, 26, 27, 28, 29]. The favorite candidate is the $P_1^{NC}-P_1$ pair, namely linear non-conforming P_1^{NC} for the velocities, and linear conforming P_1 for the elevation. This pair was first presented in [30] within the framework of two-layer models. The idea is simple: try to mimic the staggering of variables used in finite difference schemes in the finite element framework. [23] is a seminal review paper on mixed methods for finite element shallow water and initiated several works on the $P_1^{NC}-P_1$ mixed element pair. Further, this pair has been shown to be free of spurious elevation modes [27], and it has been tested it with both Eulerian and Lagrangian discretizations of advection terms [26]. In the inviscid limit, the semi-Lagrangian discretization of [26] exhibits a strong noise in the velocity field, which needs to be filtered out. The Eulerian formulation described in this paper appears to avoid this noise, due to the stabilizing effect of the upwind scheme on advection terms. The analysis of dispersion and dissipation properties is performed in [28] where a semi-analytical dispersion relation is derived on structured grids. Dissipation and dispersion relations are computed numerically on unstructured grids in [31]. It appears that the $P_1^{NC}-P_1$ pair works really well on structured grids, but is suboptimal on unstructured grids, in terms of accuracy [29] and in terms of dispersion. Recently, a new mixed element, $P_1^{DG}-P_2$, has been presented. Such an element exhibits stability and good rates of convergence for the Stokes problem and the wave equation [32] and has been proven to be LBB stable [33].

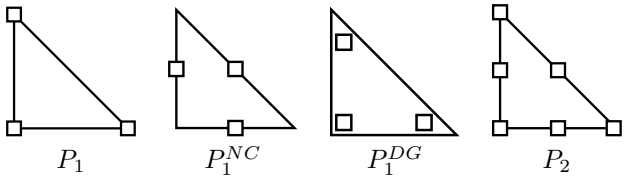

Figure 1. Sketch of the different finite elements used.

Within its space of parameters, the shallow water system has several asymptotic limit cases. In the steady viscous limit, the well-known Stokes system is found. The linear non-rotating and inviscid shallow water equations reduce to a wave equation. When Coriolis force is the leading term, we observe a geostrophic equilibrium. An almost optimal finite element method is known for each of those problems. The Stokes problem is a saddle-point problem, and the finite element formulation needs to satisfy the LBB condition, that for Galerkin formulations leads to choose a larger discrete space for velocities than for elevation, for instance P_2-P_1. The velocities and elevation have a symmetric role in the wave equation, and then using the same space for both fields is the natural solution. In the geostrophic limit, the space for velocities is the gradient of the space for elevation, and then a pair like P_1^{DG}-P_2^{DG} appears to be best suited. Of course, in real life applications, those different regimes are mixed, and a formulation at least stable in all ranges of parameters is sought. Our typical domain of application is estuarine, coastal and ocean modeling. Therefore, we do not put the focus on supercritical flows, where shocks require specific handling, while we are aware that this regime is of crucial importance for smaller scale applications.

In this paper, we focus on numerical schemes where the stabilizing strategies are only applied on the interface terms. It must be noted that it would be also possible to add stabilizing terms in the surface terms as it is usual in continuous stabilized formulations. In general, continuous stabilizing terms corresponds to adding diffusion with a coefficient depending on the element size, in a more or less consistent manner. For discontinuous methods, the interfaces integrals are estimated with an upwind bias introducing the right amount of dissipation to keep the scheme stable. We provide here a comparison between different finite element pairs that all rely on the same weak formulation: $P_1^{DG} - P_1^{DG}$, $P_1^{NC} - P_1^{NC}$, $P_1^{NC} - P_1$, $P_1^{DG} - P_1$ and $P_1^{DG} - P_2$. A sketch of those elements is given in Figure 1.

The outline of this paper is the following: section 2 explains the methodology followed to deduce all the formulations in the framework of one-dimensional linear shallow-water equations, section 3 details the formulation for the five finite element pairs considered, and in section 4, we assess the qualities and drawbacks of each formulation.

2. One-dimensional illustration of key concepts

In this section, the main concepts used in this paper are illustrated for the one-dimensional wave equation, which is the simplest idealization of the shallow water equations. The one-dimensional wave equation reads:

$$\frac{\partial^2 \eta}{\partial t^2} = gh \frac{\partial^2 \eta}{\partial x^2}, \tag{1}$$

and is equivalent to the following system of equations, known as the linearized inviscid shallow water equations in a non-rotating framework:

$$\frac{\partial \eta}{\partial t} + h\frac{\partial u}{\partial x} = 0, \tag{2}$$

$$\frac{\partial u}{\partial t} + g\frac{\partial \eta}{\partial x} = 0, \tag{3}$$

where u is the depth-averaged velocity, η the free surface elevation, h the depth at rest and g the gravitational acceleration.

We analyze the selection of mixed continuous or discontinuous spaces and the design of a suitable Riemann solver. In particular, three different finite element pairs are considered:

- $P_1 - P_1$ elements, for velocity and elevation, respectively.
- $P_1^{DG} - P_1^{DG}$ elements, the one-dimensional equivalent to the $P_1^{DG} - P_1^{DG}$ two-dimensional pair and the closest to the $P_1^{NC} - P_1^{NC}$ pair.
- $P_1^{DG} - P_1$ elements, which is the closest to two-dimensional $P_1^{NC} - P_1$ and $P_1^{DG} - P_1$.

All mixed methods rely on the same weak formulation:

$$< \frac{\partial \eta}{\partial t}\hat{\eta} > + < h\frac{\partial u}{\partial x}\hat{\eta} > = 0, \tag{4}$$

$$< \frac{\partial u}{\partial t}\hat{u} > + < g\frac{\partial \eta}{\partial x}\hat{u} > = 0, \tag{5}$$

with $< \cdot >$ denoting the integral over Ω, and $\hat{\eta}$ and $\hat{u}$ the test functions. This domain Ω is then discretized into a mesh or a collection of non-overlapping elements Ω_e. Equations (4-5) can be expressed as a sum of the integrals on each element:

$$\sum_e \left(< \frac{\partial \eta}{\partial t}\hat{\eta} >_{\Omega_e} + < h\frac{\partial u}{\partial x}\hat{\eta} >_{\Omega_e} \right) = 0, \tag{6}$$

$$\sum_e \left(< \frac{\partial u}{\partial t}\hat{u} >_{\Omega_e} + < g\frac{\partial \eta}{\partial x}\hat{u} >_{\Omega_e} \right) = 0. \tag{7}$$

Finally, in order to incorporate the local Neumann boundary condition, we integrate the gradient terms by part:

$$\sum_e \left(< \frac{\partial \eta}{\partial t}\hat{\eta} >_{\Omega_e} + hu^*\hat{\eta}\Big|_{\partial\Omega_e} - < hu\frac{\partial \hat{\eta}}{\partial x} >_{\Omega_e} \right) = 0, \tag{8}$$

$$\sum_e \left(< \frac{\partial u}{\partial t}\hat{u} >_{\Omega_e} + g\eta^*\hat{u}\Big|_{\partial\Omega_e} - < g\eta\frac{\partial \hat{u}}{\partial x} >_{\Omega_e} \right) = 0. \tag{9}$$

The values of the fields at both ends of each interval are denoted with a star superscript, because they need to be uniquely defined for both neighboring elements of the interface. The way to define u^* and η^* is the key ingredient to obtain a stable and accurate numerical formulation. On interior interfaces, for continuous test functions, the boundary integral on the one element is cancelled out by the boundary integral on the other element, but it is not the case for discontinuous test functions.

Riemann solver To deduce consistent values of fluxes u^* and η^* at the interface, relying on the characteristic structure of the equations, it is usual to introduce Riemann solver for numerical methods. Riemann solvers are a solution to deduce consistent values of fluxes. It allows to add just enough numerical dissipation to keep the scheme stable. For a scalar advection equation, using the upwind value at the interface introduces the right amount of dissipation that prevents the oscillations of the numerical solution. The Riemann solvers can be viewed as the generalization of the upwinding technique for systems of equations.

In matrix notation, the shallow water system of equations (2-3) reads:

$$\begin{pmatrix} \eta_{,t} \\ u_{,t} \end{pmatrix} + \underbrace{\begin{pmatrix} 0 & h \\ g & 0 \end{pmatrix}}_{A} \begin{pmatrix} \eta_{,x} \\ u_{,x} \end{pmatrix} = \begin{pmatrix} 0 \\ 0 \end{pmatrix}. \tag{10}$$

Let us now perform a change of variable such that the matrix A becomes diagonal. We then obtain the shallow water equations in terms of the characteristic variables:

$$\begin{pmatrix} U \\ V \end{pmatrix} = R^{-1} \begin{pmatrix} \eta \\ u \end{pmatrix} = \begin{pmatrix} \frac{\eta}{2} + u\frac{\sqrt{h/g}}{2} \\ \frac{\eta}{2} - u\frac{\sqrt{h/g}}{2} \end{pmatrix}, \tag{11}$$

where R is the matrix whose columns are eigenvectors of A:

$$R = \begin{pmatrix} 1 & 1 \\ \sqrt{g/h} & -\sqrt{g/h} \end{pmatrix}. \tag{12}$$

The system in terms of the characteristic variables corresponds to two uncoupled advection equations:

$$\begin{pmatrix} U_{,t} \\ V_{,t} \end{pmatrix} + \begin{pmatrix} \sqrt{gh} & 0 \\ 0 & -\sqrt{gh} \end{pmatrix} \begin{pmatrix} U_{,x} \\ V_{,x} \end{pmatrix} = \begin{pmatrix} 0 \\ 0 \end{pmatrix}. \tag{13}$$

We define the $*$ variables using the upwind value, that depends on the sign of the eigenvalue:

$$U^* = U^L, \quad V^* = V^R, \tag{14}$$

where the L and R superscript denote values taken at the left and right side of the interface, respectively. Expressing the original variables in terms of the characteristic ones, we get:

$$\eta = U + V, \quad u = \sqrt{\frac{g}{h}}(U - V), \tag{15}$$

and we derive the classical well-known expressions:

$$\eta^* = U^L + V^R = \{\eta\} + \sqrt{\frac{h}{g}}[u], \quad u^* = \sqrt{\frac{g}{h}}(U^L - V^R) = \{u\} + \sqrt{\frac{g}{h}}[\eta], \tag{16}$$

with $\{a\} = \frac{a^L + a^R}{2}$ the mean and $[a] = \frac{a^L - a^R}{2}$ the jump.

The same methodology can also be applied to the hybrid continuous/discontinuous finite element pair. The interface terms in the elevation equation disappear due to the continuity of the test functions, as corresponding equal contributions are added at a node by the two elements surrounding the interface. If η is continuous, (16) degenerates to:

$$\eta^* = \eta + \sqrt{\frac{h}{g}}[u], \quad u^* = \{u\}. \tag{17}$$

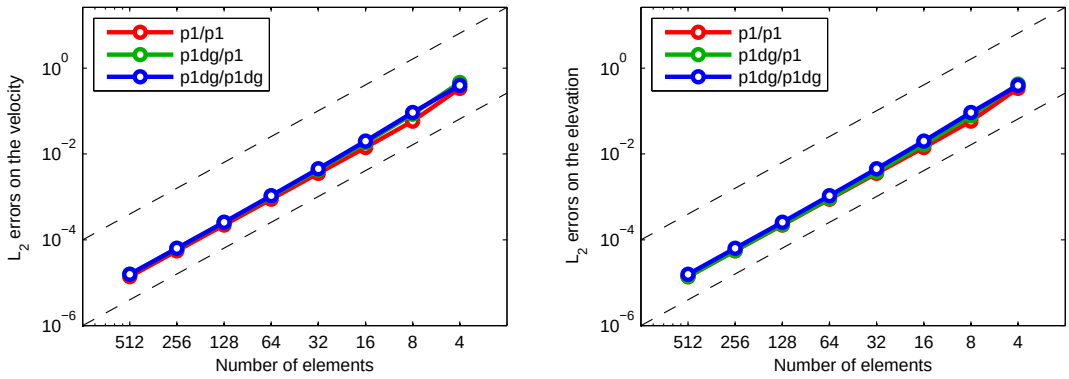

Figure 2. Convergence analysis for the wave equation with periodic boundary conditions. Second order convergence is observed on both fields for three mixed linear continuous/discontinuous discretizations.

In Figure 2, we observe second order accuracy on both elevation and velocity for the three discretizations, when we perform a convergence analysis on a wave problem with periodic boundary conditions. The optimal rate of convergence observed with the hybrid discretization $P_1^{DG} - P_1$ shows that using a mixed discontinuous-continuous pair of elements is not a priori a bad idea, even if the number of degrees of freedom is different, and so the symmetry of the discretization is broken.

3. Two-dimensional discretization of the shallow water equations

Let us now consider the complete shallow water equations including inertia terms, Coriolis effects, viscous terms, and both wind and bottom stresses. It is usual to disctinct two classical formulations, when deriving a numerical scheme. On the one hand, the conservative formulation in terms of the total depth H and the transport $H\boldsymbol{u}$ reads:

$$\frac{\partial H}{\partial t} + \boldsymbol{\nabla} \cdot \big(H\boldsymbol{u}\big) = 0, \tag{18}$$

$$\frac{\partial H\boldsymbol{u}}{\partial t} + \boldsymbol{\nabla} \cdot \big(H\boldsymbol{u}\boldsymbol{u}\big) + f\boldsymbol{k} \times \big(H\boldsymbol{u}\big) + gH\boldsymbol{\nabla}\big(H - h\big) = \boldsymbol{\nabla} \cdot \Big(H\nu\big(\boldsymbol{\nabla}\boldsymbol{u}\big)\Big) + \frac{\boldsymbol{\tau^s} + \boldsymbol{\tau^b}}{\rho}, \tag{19}$$

with h the depth at rest, f is the Coriolis factor, $\boldsymbol{k}$ the vertical unit vector, $\boldsymbol{\tau^s}$ and $\boldsymbol{\tau^b}$ the surface and bottom stresses, ρ the density and ν the eddy viscosity. On the other hand, the non-conservative formulation in terms of free-surface elevation η (with $H = h+\eta$) and velocity $\boldsymbol{u}$ reads:

$$\frac{\partial \eta}{\partial t} + \boldsymbol{\nabla} \cdot \Big(\big(h + \eta\big)\ \boldsymbol{u}\Big) = 0, \tag{20}$$

$$\frac{\partial \boldsymbol{u}}{\partial t} + \boldsymbol{u} \cdot \big(\boldsymbol{\nabla}\boldsymbol{u}\big) + f\boldsymbol{k} \times \boldsymbol{u} + g\boldsymbol{\nabla}\eta = \frac{1}{H}\boldsymbol{\nabla} \cdot \Big(H\nu\big(\boldsymbol{\nabla}\boldsymbol{u}\big)\Big) + \frac{\boldsymbol{\tau^s} + \boldsymbol{\tau^b}}{\rho H}. \tag{21}$$

It is customary to use the conservative formulation when deriving finite difference schemes for the shallow water equations, in order to obtain a conservative numerical scheme. However, in

a continuous framework, both formulation are strictly equivalent from a mathematical point of view.

In this paper, we will use the non-conservative form of the shallow water equations to derive the weak formulation, with a nonlinear approximate Riemann solver deduced from the conservative form of the same equations. This approach might appear a little exotic but it is motivated by the following facts. Firstly, it is natural to write a Riemann solver in terms of fluxes of quantities to be conserved. Secondly, it would be also attractive to write a weak conservative formulation but in this case, the elevation gradient term has to be split in two parts, a flux term and a source term:

$$gH\boldsymbol{\nabla}\big(H-h\big)=\frac{g\boldsymbol{\nabla}\big(H^2-h^2\big)}{2}-g\big(H-h\big)\boldsymbol{\nabla}h. \tag{22}$$

With discontinuous Galerkin methods, both terms are not treated in the same way. It has been shown that the scheme may exhibit nonphysical oscillations if the integration is not accurate enough [13]. We then decide to implement a weak non-conservative formulation because it seems more efficient and robust in the considered numerical discretization.

Non-conservative weak formulation The weak form of this non-conservative formulation follows:

$$\sum_e\left(<\frac{\partial\eta}{\partial t}\,\hat{\eta}>_{\Omega_e}+<\boldsymbol{\nabla}\cdot\Big((h+\eta)\,\boldsymbol{u}\Big)\,\hat{\eta}>_{\Omega_e}\right)=0\ , \tag{23}$$

$$\begin{aligned}\sum_e\Bigg(&<\frac{\partial\boldsymbol{u}}{\partial t}\cdot\hat{\boldsymbol{u}}>_{\Omega_e}+<\boldsymbol{u}\cdot\big(\boldsymbol{\nabla}\boldsymbol{u}\big)\cdot\hat{\boldsymbol{u}}>_{\Omega_e}+<f(\boldsymbol{k}\times\boldsymbol{u})\cdot\hat{\boldsymbol{u}}>_{\Omega_e}+g<\big(\boldsymbol{\nabla}\eta\big)\cdot\hat{\boldsymbol{u}}>_{\Omega_e}\Bigg)\\&=\sum_e\left(<\frac{1}{H}\boldsymbol{\nabla}\cdot\Big(H\nu\big(\boldsymbol{\nabla}\boldsymbol{u}\big)\Big)\cdot\hat{\boldsymbol{u}}>_{\Omega_e}+<\frac{\boldsymbol{\tau^s}+\boldsymbol{\tau^b}}{\rho H}\cdot\hat{\boldsymbol{u}}>_{\Omega_e}\right).\end{aligned} \tag{24}$$

Again integrating by parts, we get:

$$\sum_e\left(<\frac{\partial\eta}{\partial t}\,\hat{\eta}>_{\Omega_e}+\ll(h+\eta^*)u_n^*\hat{\eta}\gg_{\partial\Omega_e}-<(h+\eta)\,\boldsymbol{u}\cdot\boldsymbol{\nabla}\hat{\eta}>_{\Omega_e}\right)=0\ , \tag{25}$$

$$\begin{aligned}&\sum_e\Bigg(<\frac{\partial\boldsymbol{u}}{\partial t}\cdot\hat{\boldsymbol{u}}>_{\Omega_e}+\ll u_n^*\boldsymbol{u}^*\cdot\hat{\boldsymbol{u}}\gg_{\partial\Omega_e}-<\boldsymbol{\nabla}\cdot\big(\boldsymbol{u}\hat{\boldsymbol{u}}\big)\cdot\boldsymbol{u}>_{\Omega_e}\\&\qquad+<f(\boldsymbol{k}\times\boldsymbol{u})\cdot\hat{\boldsymbol{u}}>_{\Omega_e}+g\ll\eta^*\hat{u}_n\gg_{\partial\Omega_e}-g<\eta\big(\boldsymbol{\nabla}\cdot\hat{\boldsymbol{u}}\big)>_{\Omega_e}\Bigg)\\=\ &\sum_e\Bigg(\ll\nu\left\{\frac{\partial\boldsymbol{u}}{\partial n}\right\}\cdot\hat{\boldsymbol{u}}\gg_{\partial\Omega_e}-<\nu\big(\boldsymbol{\nabla}\boldsymbol{u}\big):\big(\boldsymbol{\nabla}\hat{\boldsymbol{u}}\big)>_{\Omega_e}\\&\qquad+<\nu\frac{1}{H}\big(\boldsymbol{\nabla}H\big)\cdot\big(\boldsymbol{\nabla}\boldsymbol{u}\big)\cdot\hat{\boldsymbol{u}}>_{\Omega_e}+<\frac{\boldsymbol{\tau^s}+\boldsymbol{\tau^b}}{\rho H}\cdot\hat{\boldsymbol{u}}>_{\Omega_e}\Bigg).\end{aligned} \tag{26}$$

The vector quantities multiplied by the outward normal are denoted with a n subscript. Once more, the variables used in the boundary integrals are doubled-valued, and are denoted

with a star superscript. However, for the diffusive flux, it is natural to take the centered values denoted by $\{\cdot\}$, as diffusive phenomena are isotropic. As explained in the introduction, a specific treatment is needed to obtain a stable and accurate discretization of the diffusive term when using discontinuous elements for the velocities. In this case, the following term is added in the right-hand side of equation (26):

$$\sum_e \left(- \ll \sigma \hat{\boldsymbol{u}} \cdot [\boldsymbol{u}] \gg_{\partial\Omega_e} \right), \tag{27}$$

with σ a penalization parameter defined as:

$$\sigma = \frac{\nu(p+1)(p+2)}{h}, \tag{28}$$

with h a typical length scale of the element, and p the polynomial order of the finite element space. This value of the penalization parameter has been proposed in [34].

Approximate nonlinear Riemann solver Unfortunately, a Riemann solver cannot be applied on the non-conservative form of the equations, as they are not in flux form. For that purpose, we use the conservative form (18-19) of the shallow water equations to derive the Riemann solver, where the dissipation, Coriolis and diffusion terms are neglected. Considering u the velocity normal to the interface, and v the velocity tangent to the interface, the flux reads:

$$F = \begin{pmatrix} F_H \\ F_{Hu} \\ F_{Hv} \end{pmatrix} = \begin{pmatrix} Hu \\ Huu + \frac{g}{2}H^2 \\ Huv \end{pmatrix}. \tag{29}$$

The exact Riemann solver requires the resolution of a nonlinear problem at each integration point. It is usually prefered to use an approximate Riemann solver. In order to deduce such an approximate Riemann solver, the next step consists in linearizing the fluxes. The Jacobian matrix of the fluxes is:

$$J = \begin{pmatrix} 0 & 1 & 0 \\ -u^2 + gH & 2u & 0 \\ -uv & v & u \end{pmatrix}. \tag{30}$$

Finally, we use the Roe averages to obtain a approximate Jacobian matrix $J_{\text{linearized}}$, as in classical textbooks [35]. This rule can be deduced easily from the Rankine-Hugoniot relation:

$$J_{\text{linearized}} \begin{pmatrix} [H] \\ [Hu] \\ [Hv] \end{pmatrix} = [F]. \tag{31}$$

As the first line of the Jacobian matrix is linear, the Rankine-Hugoniot relation leads to an underdetermined system. To obtain a unique solution of the system, we select the arithmetic mean for H, and we get the classical Roe averages, with the help of symbolic calculus:

$$H_{\text{Roe}} = \{H\}, \tag{32}$$

$$u_{\text{Roe}} = \frac{u_L\sqrt{H_L} + u_R\sqrt{H_R}}{\sqrt{H_L} + \sqrt{H_R}}, \tag{33}$$

$$v_{\text{Roe}} = \frac{v_L\sqrt{H_L} + v_R\sqrt{H_R}}{\sqrt{H_L} + \sqrt{H_R}}. \tag{34}$$

By substituting (H, u, v) by $(H_{\text{Roe}}, u_{\text{Roe}}, v_{\text{Roe}})$ in the Jacobian, the approximate Riemann values of the conservative variables can be deduced as the exact solution of the linearized problem, as shown in the illustrative one-dimensional wave equation. With the help of symbolic calculus, the values of the conservative and non-conservative variables at the interface are given by:

$$H^* = \{H\} + \frac{1}{\sqrt{gH_{\text{Roe}}}} \left([Hu] - u_{\text{Roe}} [H]\right), \tag{35}$$

$$(Hu)^* = \{Hu\} + \frac{1}{\sqrt{gH_{\text{Roe}}}} \left(u_{\text{Roe}} [Hu] - u_{\text{Roe}}^2 [H]\right), \tag{36}$$

$$(Hv)^* = (Hv)_{\text{upwind}} + v_{\text{Roe}}(\{H\} - H_{\text{upwind}}) + \frac{1}{\sqrt{gH_{\text{Roe}}}} \left(v_{\text{Roe}} [Hu] - u_{\text{Roe}} v_{\text{Roe}} [H]\right) \tag{37}$$

$$\eta^* = H^* - h, \tag{38}$$

$$u^* = \frac{(Hu)^*}{H^*}, \tag{39}$$

$$v^* = \frac{(Hv)^*}{H^*}. \tag{40}$$

4. Mesh refinement analysis

Description of the meshes

Convergence tests are carried out with a family of 25 meshes each time adapted to the reference solution of the flow except for both wave problems where uniform unstructured meshes are used. We use adapted meshes rather than uniform meshes, since some of the studied flows have western boundary layers that need to be sufficiently resolved to see the asymptotic convergence behavior of the schemes. Using uniform meshes would require many more elements to observe asymptotic behavior. The greatest eigenvalue of the elevation field's Hessian matrix is used as an a priori error estimator, since with linear elements, the error is dominated by the quadratic component of the solution. We define a reference edge length field δ as:

$$\delta(x, y) = \sqrt{\frac{\int_\Omega e d\Omega}{e(x, y)}}. \tag{41}$$

where $e(x, y)$ is the norm of the greatest eigenvalue of the Hessian matrix of the elevation field. The meshes are generated using Gmsh [36], where we use $h\delta$ as edge length field, with h a constant over the domain. The generated meshes have therefore about $1/(ah^2)$ elements, with $a \approx 0.8$ the typical area of a triangle whose edge have unit length. In Figure 3, we show the reference edge length field δ and five of the corresponding meshes for the nonlinear Munk testcase. The 9^{th} finest mesh of each family, made of about 2500 triangles, are shown in Figures 5 to 9. Reference solutions are obtained using highly accurate P_3^{DG}-P_2^{DG} scheme for Stokes problem and P_3^{DG}-P_3^{DG} scheme for all other problems, using the same discrete formulation and time-stepping algorithm on the finest mesh used for the convergence tests.

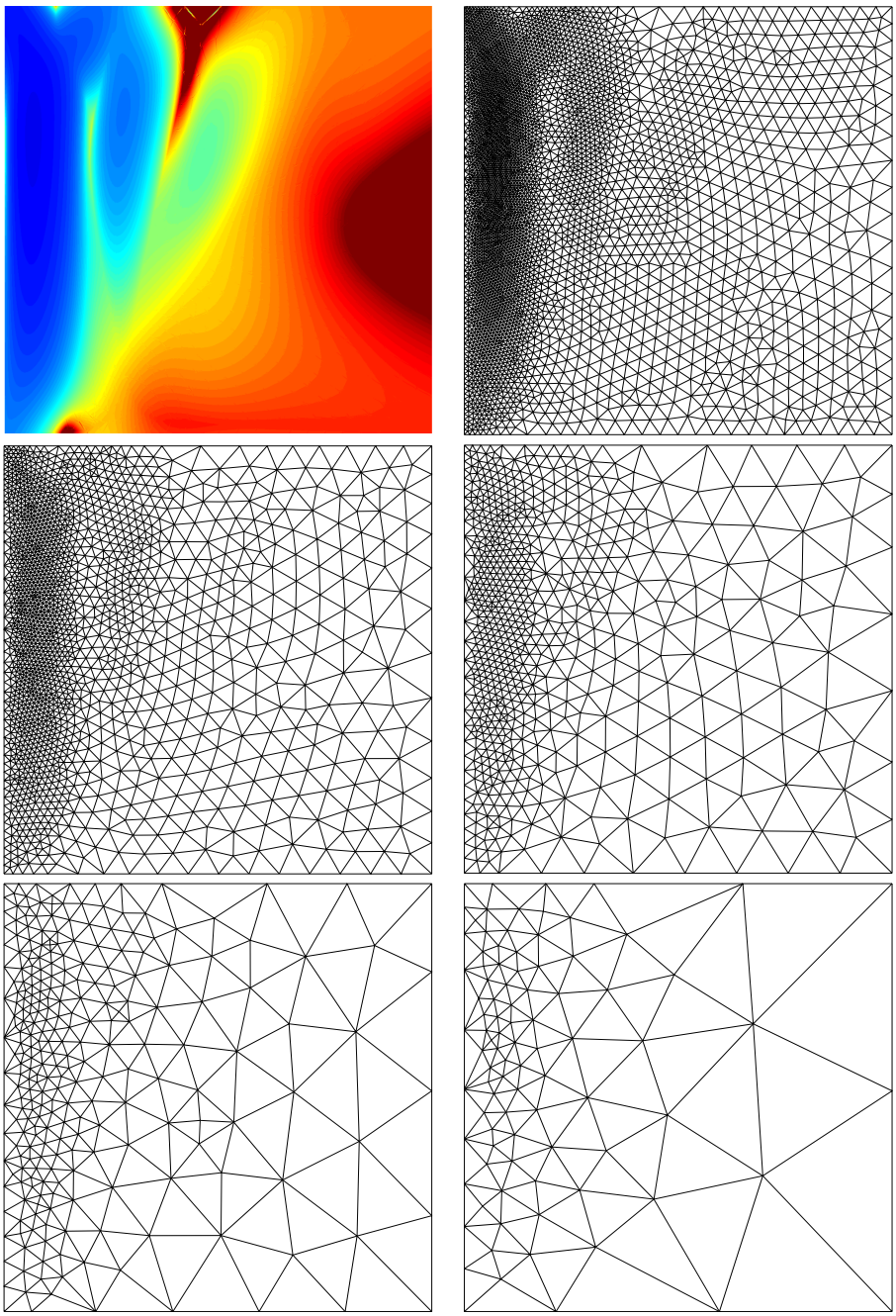

Figure 3. Sketch of the edge-length field δ and five corresponding meshes for the nonlinear Munk testcase.

	L $[m]$	H $[m]$	g $[ms^{-2}]$	f $[s^{-1}]$	γ $[s^{-1}]$	ν $[ms^{-2}]$	Nonlinear advection and free-surface terms
Unsteady wave	10^6	10^3	9.81	0	0	0	no
Steady wave	10^6	10^3	9.81	0	10^{-6}	0	no
Stokes	10^6	10^3	9.81	0	0	10^4	no
Geostrophic equilibrium	10^6	10^3	9.81	10^{-4}	0	0	no
Stommel gyre	10^6	10^3	9.81	10^{-4}	10^{-6}	0	no
Munk gyre	10^6	10^3	9.81	10^{-4}	0	10^4	no
Advective Stommel gyre	10^6	10^3	9.81	10^{-4}	5×10^{-7}	0	yes
Advection Munk gyre	10^6	10^3	9.81	10^{-4}	0	3000	yes

Table I: Summary of physical parameters for each of the testcases.

Presentation of the testcases

Considering typical oceanic and coastal flows, we define a serie of testcases, with the corresponding relevant meshes, detailed in Figures 4, 5, 6, 7, 8 and 9. The objective is to fairly compare the proposed finite element pairs. Three limit flow states of the shallow water system, namely geostrophy, wave propagation and viscosity, are tested separately, and then the complexity of the problem is increased toward more realistic computations. Each of these flows develops in a square basin of 1000×1000 km.

Some of the testcases use a zonal wind stress, defined as:

$$\boldsymbol{\tau^s} = 0.1 \times \sin\left(\pi \frac{y}{L}\right) \boldsymbol{e}_x, \tag{42}$$

inducing a clockwise circulation, and a linear dissipation term defined as:

$$\boldsymbol{\tau^b} = -\rho h \gamma \boldsymbol{u}. \tag{43}$$

For all the testcases, we use slipping coasts. The testcases with viscosity need a second boundary condition, so we cancel out the normal flux of tangential velocity, and we compute the normal flux of normal velocity with the interior value of the velocity.

Table I summarizes the physical parameters that define each of the testcases.

Wave equation As a first testcase, we consider the linear wave equation:

$$\frac{\partial \eta}{\partial t} + \boldsymbol{\nabla} \cdot \left(h \boldsymbol{u}\right) = 0, \tag{44}$$

$$\frac{\partial \boldsymbol{u}}{\partial t} + g \boldsymbol{\nabla} \eta = 0. \tag{45}$$

It is the simplest approximation of the shallow water equations. Wave phenomena are the leading effects in small scale low Froude number flows. A gaussian is given as initial condition for the elevation, and we observe the solution after one hour, so that the wave crest has covered more than 350 km. A fourth order explicit Runge-Kutta scheme is used to progress in time, with a time step corresponding to the CFL condition, ensuring that the solution is converged in time.

As the goal of this paper is to show which finite element pair may be unstable or exhibit a lack of convergence, a steady testcase is much tougher. Indeed, the spurious modes that can appear in a finite element discretization are fully excited in steady solution, while they appear progressively in a time dependent problem. We then simulate a steady flow where wind forcing is balanced by linear dissipation:

$$\boldsymbol{\nabla} \cdot (h\boldsymbol{u}) = 0, \tag{46}$$

$$g\boldsymbol{\nabla}\eta = \frac{\boldsymbol{\tau^s}}{\rho h} - \gamma u, \tag{47}$$

with $\gamma = 10^{-6}\ s^{-1}$.

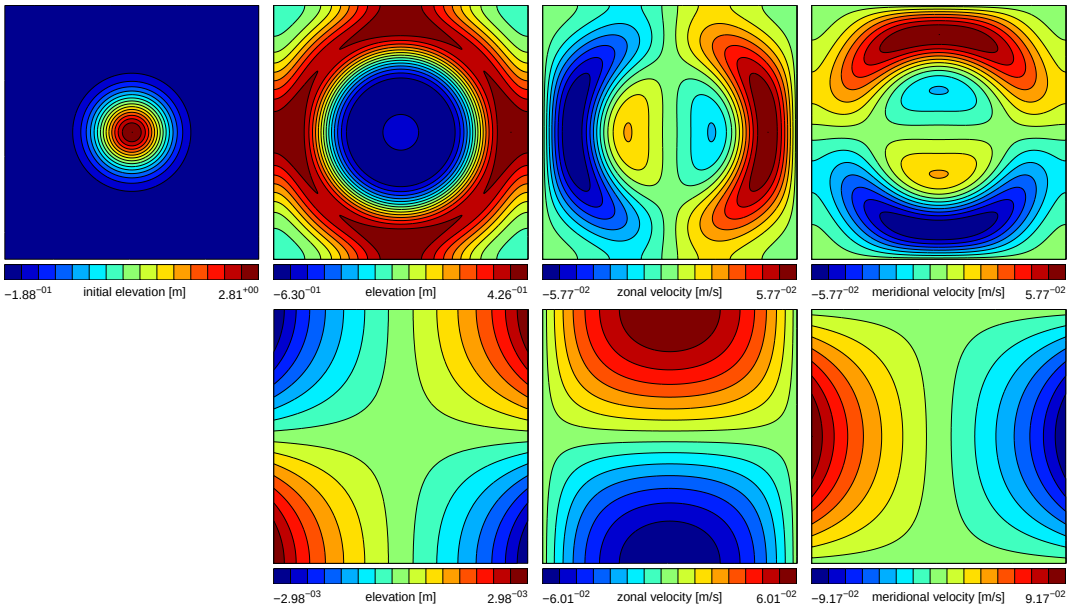

Figure 4. Sketch of the elevation and velocity fields for the unsteady (top) and steady (bottom) wave testcases.

Stokes flow The Stokes equations represent creeping flows, where inertial terms are negligible compared to viscous terms. This problem is difficult to solve numerically, because the incompressibility equation acts as a constrain on the velocity field. In order to obtain a mixed discrete formulation that defines a well-posed problem, it is mandatory to stabilize the discrete formulation or to define the mixed discretization space in such a way that the LBB condition is satisfied [37]. From a practical point of view, the discrete space for elevation/pressure must be small enough compared to the discrete space for velocities, in a usual mixed formulation. The wind forcing now balances the viscous dissipation:

$$\boldsymbol{\nabla} \cdot (h\boldsymbol{u}) = 0, \tag{48}$$

$$g\boldsymbol{\nabla}\eta = \frac{\boldsymbol{\tau^s}}{\rho h} + \boldsymbol{\nabla} \cdot (\nu \boldsymbol{\nabla} \boldsymbol{u}), \tag{49}$$

with $\nu = 10^4\ ms^{-2}$.

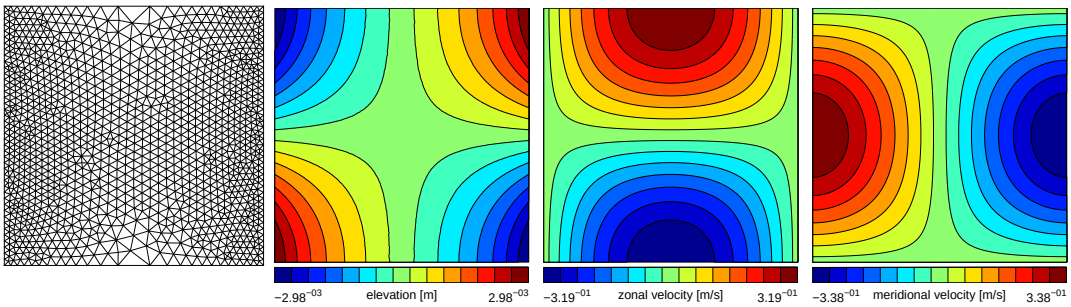

Figure 5. Typical mesh and sketch of the elevation and velocity fields for the Stokes testcase.

Geostrophic equilibrium Geophysical flows experience the Coriolis force, due to the rotation of the frame of reference. It is one of the leading terms in the large scale shallow water equations. We test the ability of the different methods to maintain a linear geostrophic equilibrium, where the Coriolis force is in balance with the elevation gradient. As there is no dissipation, a good numerical scheme should maintain this equilibrium for a long time. The elevation field is a gaussian bell of three meter height. Coriolis parameter f is $10^{-4}s^{-1}$ in the whole domain. A third-order implicit-explicit Runge-Kutta method is used to progress in time, with a time step corresponding to the CFL criterion on advection, the terms related to gravity waves being treated implicitly. The flow satisfies the following equations:

$$\frac{\partial \eta}{\partial t} + \boldsymbol{\nabla} \cdot (h\boldsymbol{u}) = 0, \tag{50}$$

$$\frac{\partial \boldsymbol{u}}{\partial t} + f\boldsymbol{k} \times \boldsymbol{u} + g\boldsymbol{\nabla}\eta = 0. \tag{51}$$

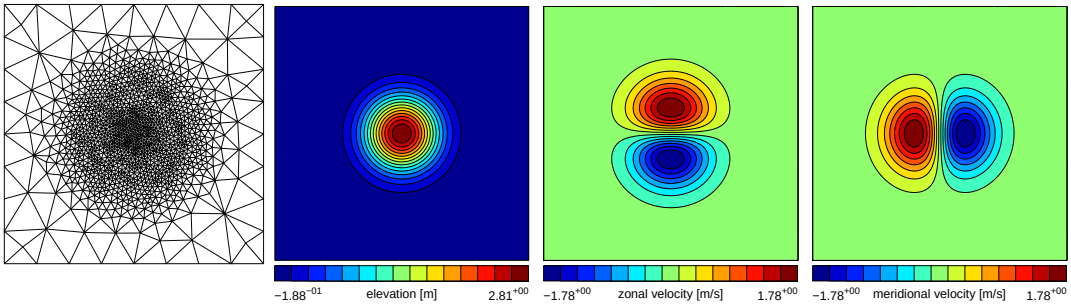

Figure 6. Typical mesh and sketch of the elevation and velocity fields for the geostrophic equilibrium testcase.

Stommel gyre A time dependent problem may not exhibit all the troubles that can be generated by the discretization. The steady counterpart to the geostrophic equilibrium is the Stommel gyre. The Coriolis effect is taken into account using the β-plane approximation, $f = f_0 + \beta y$, with $f_0 = 10^{-4}\ s^{-1}$ and $\beta = 2 \times 10^{-11}\ m^{-1}s^{-1}$, corresponding to a midlatitude domain in the northern hemisphere. The flow is forced by the wind stress defined at equation (42), that induces a clockwise circulation, while a linear dissipation with coefficient $\gamma = 10^{-6}\ s^{-1}$ balances the forcing. The variation of this Coriolis parameter induces Rossby waves that propagate westward and generate a strong boundary current. The flow satisfies the following equations:

$$\frac{\partial \eta}{\partial t} + \boldsymbol{\nabla} \cdot (h\boldsymbol{u}) = 0, \tag{52}$$

$$\frac{\partial \boldsymbol{u}}{\partial t} + f\boldsymbol{k} \times \boldsymbol{u} + g\boldsymbol{\nabla}\eta = \frac{\boldsymbol{\tau^s}}{\rho h} - \gamma \boldsymbol{u}. \tag{53}$$

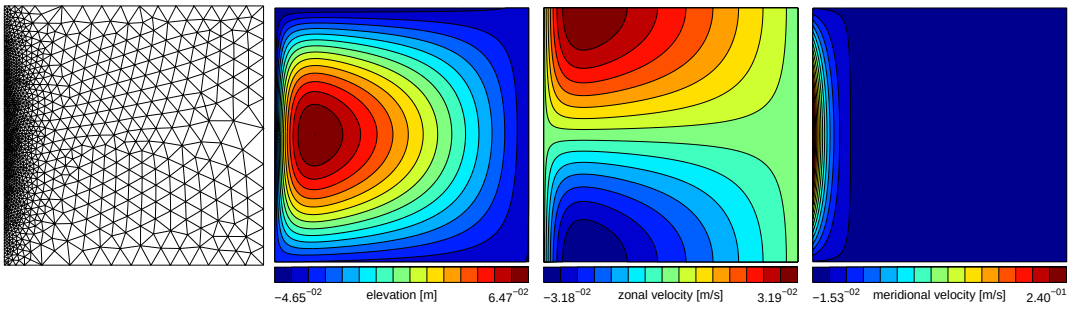

Figure 7. Typical mesh and sketch of the elevation and velocity fields for the Stommel gyre testcase.

Munk gyre The Munk gyre testcase is similar to the Stommel one, the difference is that now the wind forcing is balanced by viscous dissipation rather than linear damping. The viscosity parameter is constant in space and taken as $\nu = 10^4\ ms^{-2}$. The flow satisfies the following equations:

$$\frac{\partial \eta}{\partial t} + \boldsymbol{\nabla} \cdot (h\boldsymbol{u}) = 0, \tag{54}$$

$$\frac{\partial \boldsymbol{u}}{\partial t} + f\boldsymbol{k} \times \boldsymbol{u} + g\boldsymbol{\nabla}\eta = \frac{\boldsymbol{\tau^s}}{\rho h} + \boldsymbol{\nabla} \cdot (\nu \boldsymbol{\nabla} \boldsymbol{u}). \tag{55}$$

In fact, this testcase is often easier to solve by all numerical schemes. The viscous terms are typical elliptic contributions removing most of the troubles that may pollute the inviscid solution.

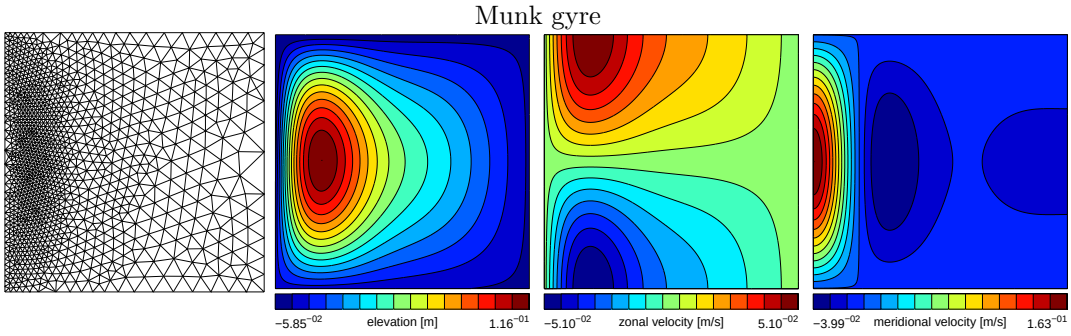

Figure 8. Typical mesh and sketch of the elevation and velocity fields for the Munk gyre testcase.

Nonlinear problems Finally, we incorporate the advection terms in both the Stommel and the Munk gyre problems. The first one is inviscid, satisfying the system:

$$\frac{\partial \eta}{\partial t} + \boldsymbol{\nabla} \cdot ((h+\eta)\boldsymbol{u}) = 0, \tag{56}$$

$$\frac{\partial \boldsymbol{u}}{\partial t} + \boldsymbol{u} \cdot \boldsymbol{\nabla} \boldsymbol{u} + f\boldsymbol{k} \times \boldsymbol{u} + g\boldsymbol{\nabla}\eta = \frac{\boldsymbol{\tau^s}}{\rho H} - \gamma \boldsymbol{u}, \tag{57}$$

with the same Coriolis factor as the two previous testcases, and a linear dissipation of coefficient $\gamma = 5 \times 10^{-7}$. The second one is viscous, with viscosity $\nu = 3000\ ms^{-2}$:

$$\frac{\partial \eta}{\partial t} + \boldsymbol{\nabla} \cdot ((h+\eta)\boldsymbol{u}) = 0, \tag{58}$$

$$\frac{\partial \boldsymbol{u}}{\partial t} + \boldsymbol{u} \cdot \boldsymbol{\nabla} \boldsymbol{u} + f\boldsymbol{k} \times \boldsymbol{u} + g\boldsymbol{\nabla}\eta = \frac{\boldsymbol{\tau^s}}{\rho H} + \frac{1}{H}\boldsymbol{\nabla} \cdot (H\nu \boldsymbol{\nabla} \boldsymbol{u}). \tag{59}$$

The numerical handling of the advection term is not simple, and requires a suitable numerical strategy. However, some difficulties appearing in the problems without advection terms are sometimes solved by the diffusion introduced within the discretization of those advection terms.

In realistic applications, the advection processes can be the leading phenomena in some areas while being almost negligible in other areas for a single computation. Therefore, both limit cases, with and without advection, have to be solved accurately. Unfortunately, it is not the case for some schemes that would appear to be attractive otherwise.

Numerical results

To quantify the errors for all finite element pairs for each testcase, convergence studies are given in Figures 10 and 11. The left panels show the diagrams for the elevation field, while the right panels show the diagrams for velocities. The dots represent the values of the L_2 norm of the discretization error normalized by the range of the field. The slopes of the linear mean-square regression, representing the orders of accuracy, are given in the legends. To further quantify the error, the best solution that can be obtained, in the sense of the L_2 norm is traced in continuous line. It is defined as the error in L_2 norm between the reference solution and the L_2 projection of this reference solution onto the finite element space defined with the current mesh.

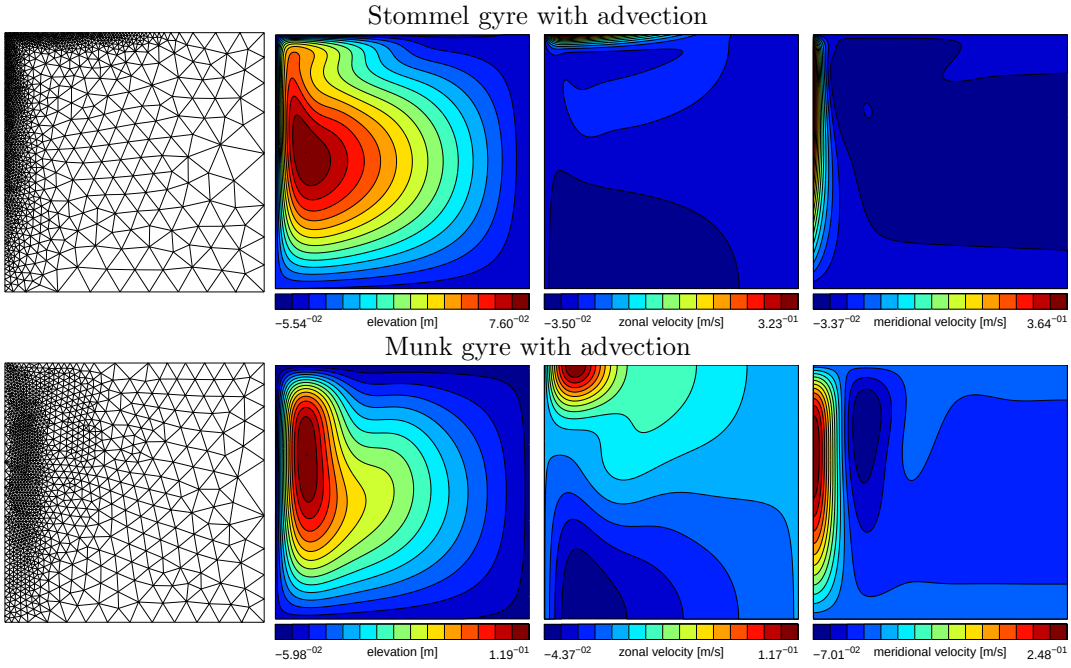

Figure 9. Typical meshes and sketch of the elevation and velocity fields for the nonlinear Stommel (top) and Munk (bottom) gyres.

A few conclusions may be drawn directly. The velocity fields of P_1^{NC}-P_1 and P_1^{DG}-P_1 pairs lack of convergence in the absence of viscosity. P_1^{NC}-P_1 was known to have such a behavior [29, 26]. This trouble is related to the wave component of the shallow water problem. The velocity field has too many degrees of freedom, and a velocity noise can develop, that has little influence on the elevation field. This noise component is bounded, as we still observe convergence at a reduced rate. The boundedness of the noise implies that the noise is not an eigenvector lying in the nullspace of the discrete operator, hence this noise was not shown by the study in [27]. This mode depends on the structure of the mesh. With structured meshes made of squares divided in half, optimal convergence is observed for both fields [29]. The same observation has been made for dispersion and dissipation properties, where analytical considerations on structured grids give promising results [28, 38, 39], while numerical analysis on unstructured grids shows disappointing results [31]. Using structured meshes of squares divided in four where all triangles are not topologically identical, a relatively structured noise appears (see Figure 12). It is therefore possible to carry out spectral analysis as in [38, 39], to further characterize the behavior of this pair.

The $P_1^{DG}-P_2$ pair demonstrates its very good properties in the vast majority of the testcases. An optimal rate of convergence for velocities is observed in all the testcases, and furthermore the solution is always quite close to the optimal solution for this element (i.e. close to the solid line in the right panels of Figures 10 and 11). Optimal convergence rate for elevation is obtained for the time-dependent testcases, where initial condition was third order accurate,

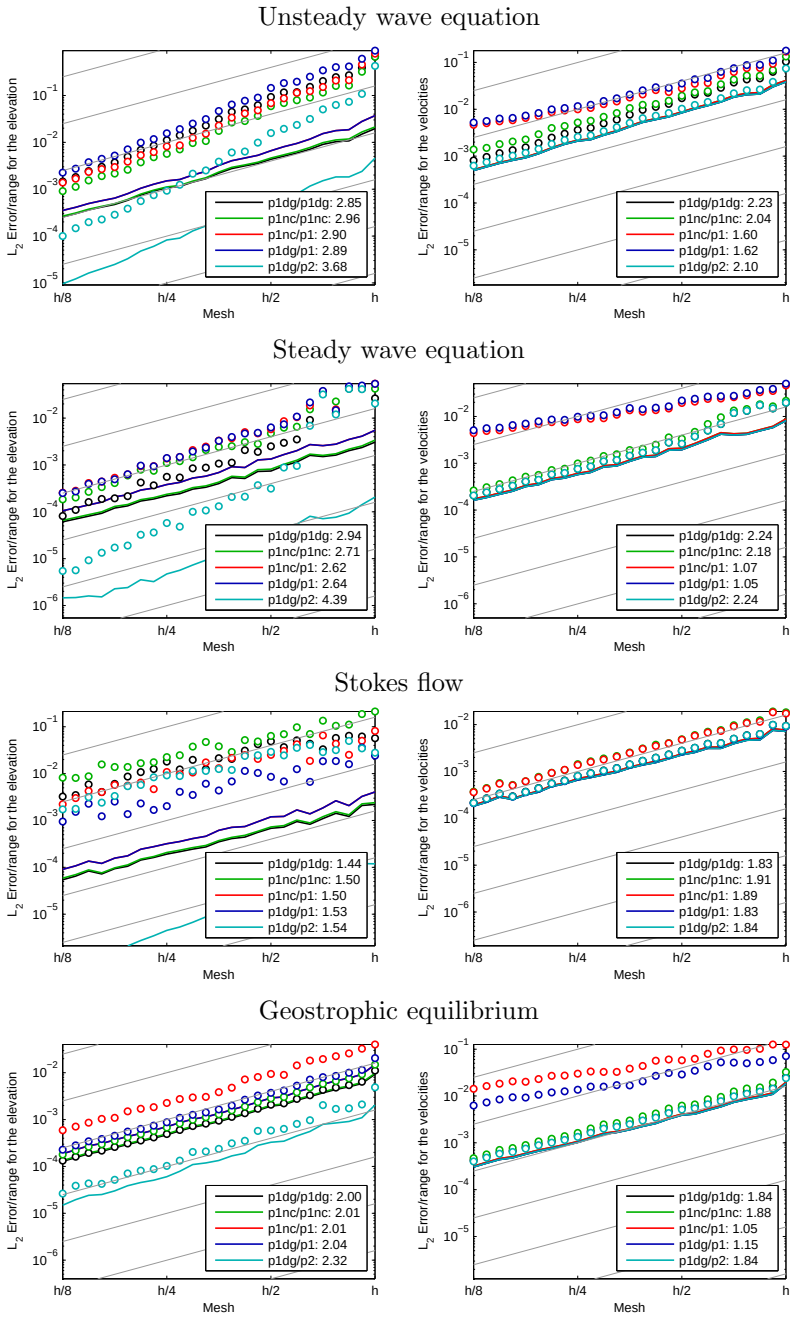

Figure 10. Convergence analysis. The circles denote the L_2 error, while continuous lines indicate the error of the best solution that the discrete space can represent. The light grey lines indicates reference second ordre convergence. The errors are plotted against the ratio h between the edge length and the reference size field. The number of elements scales as h^2.

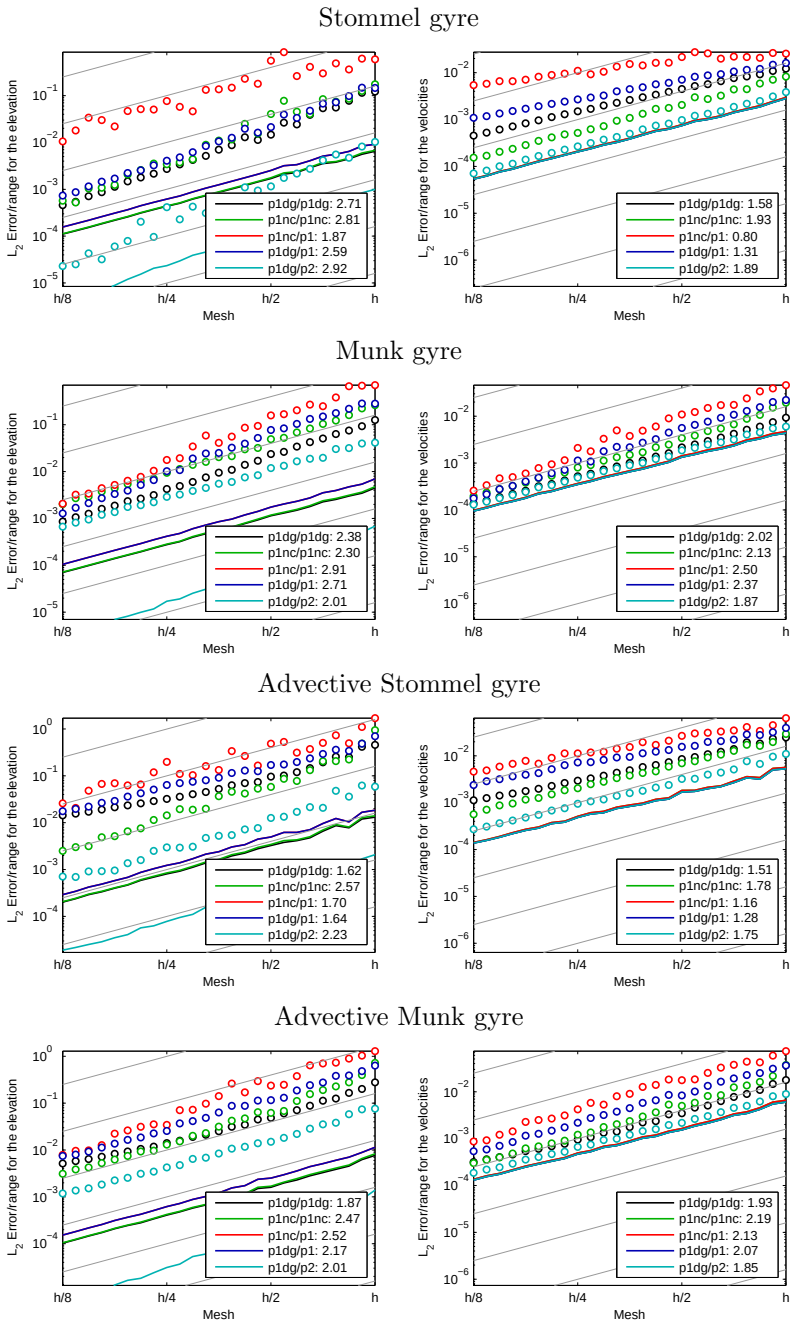

Figure 11. Convergence analysis. The circles denote the L_2 error, while continuous lines indicate the error of the best solution that the discrete space can represent. The light grey lines indicates reference second ordre convergence. The errors are plotted against the ratio h between the edge length and the reference size field. The number of elements scales as h^2.

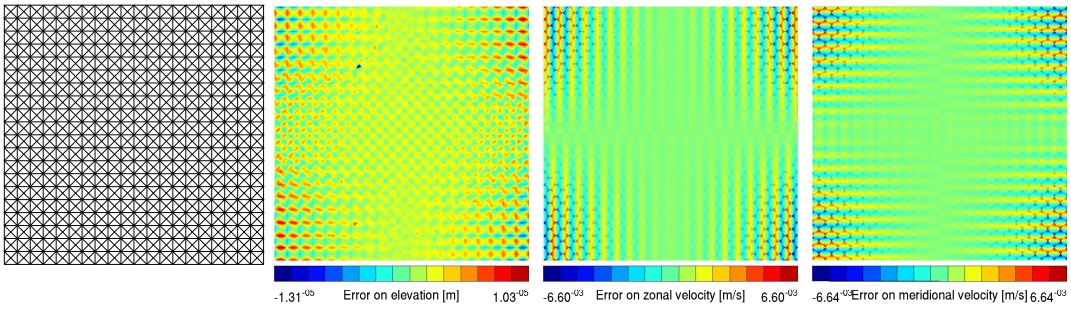

Figure 12. Sketch of the error for the steady wave problem, using P_1^{NC}-P_1 on the "Union Jack" mesh.

but also for the linear Stommel gyre. The latter can be explained as the functional spaces are optimally designed for geostrophy, as the gradient of the P_2 space exactly lies in the P_1^{DG} space. The nonlinearities seem to slightly deteriorate the accuracy of the solution to second order as the velocity and elevation fields are much more coupled.

For the Stokes flow, all the pairs exhibit second order accuracy for velocities, and a 1.5 order of convergence for elevations. Our discontinuous Galerkin method applied to the Stokes equations must be related to that from [40] and [41], where interface fluxes are deduced from an artificial incompressibility Riemann problem. The time-dependent shallow water equations do not exhibit a solenoidal constrain for the velocity field, but in the steady limit, we recover an incompressibility constrain. Therefore, we use the surface gravity wave speed $\sqrt{gh}$ where an arbitrary wave velocity c is used in [40]. An additionnal difference is that the BRMPS method (refered as *Bassi et al. [13]* in the review [15]) is used to treat the diffusion terms, where we use an incomplete interior penalty method (IIPG method in the book [17]). Still with DG, the same behavior is observed in [42], using local-DG formulation, and proof that first and second order accuracy are expected for pressures and velocities, respectively, is given. All the finite element pairs do converge, but it cannot be excluded that some of them exhibit pressure modes on specific grids.

When Coriolis comes into play, the P_1^{DG}-P_1^{DG} pair lacks almost half an order of convergence for velocities. The velocity field in geostrophic equilibrium with a piecewise linear elevation field is piecewise constant. Then, interface terms are needed in the formulation to smooth the velocity field. Indeed, flux terms exist for the normal velocity, but not for the tangent velocity. Therefore, jumps on tangent velocities are allowed by the formulation, as shown in Figure 13 for the inviscid Stommel problem on a structured grid. The same half order of convergence is lost with second order shape functions ($P_2^{DG} - P_2^{DG}$) on the same meshes.

The nonlinear advection terms do not significantly change the behavior of the different schemes. For the P_1^{DG}-P_1^{DG}, in the inviscid case, the lack of convergence on the velocity field is propagated in the elevation field. The P_1^{NC}-P_1 and P_1^{DG}-P_1 velocity solutions are slightly smoothened by the numerical dissipation associated with the handling of the advective term, but the optimal convergence rates are not recovered. High Froude number are needed for the interface dissipation to be large enough to smooth the solution and recover the optimal behavior. Indeed, the Gulf of Mexico testcase from [26] corresponds to a maximum Froude number of more than 1/4, and the Williamson's testcases on the sphere, that were solved with

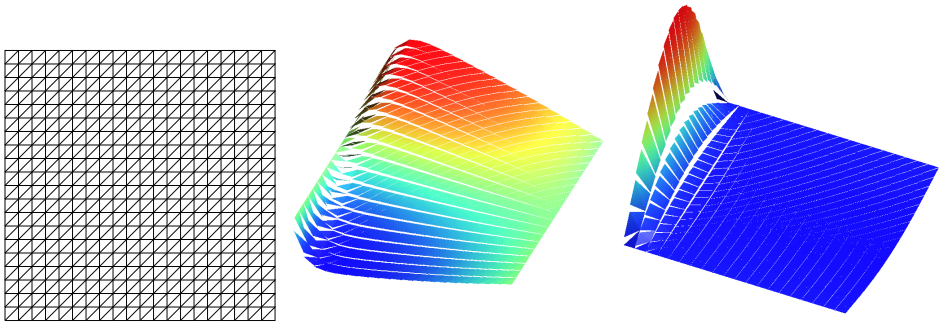

Figure 13. Zonal (center) and meridional (right) velocity field of the linear Stommel problem solved with the P_1^{DG}-P_1^{DG} pair on a structured mesh (left).

optimal convergence rate in [43], are also advection dominated, with Froude numbers as high as 1/10.

The P_1^{NC}-P_1^{NC} pair has an overall quite encouraging behavior. The pair shows optimal convergence rate in all the testcases, except the Stokes flow. Those rates are never lower than the rates observed with the P_1^{DG}-P_2 pair. The error values are slightly higher than those for P_1^{DG}-P_2 or P_1^{DG}-P_1^{DG} (when optimal rates are observed), but it must be noticed that it only requires half the number of degrees of freedom of the discontinuous Galerkin method. Moreover, the P_1^{NC} element naturally treats diffusion terms, while P_1^{DG} requires interior penalty method.

5. Conclusion

We give an unified framework to define finite element formulations of the shallow water equations with continuous, discontinuous or partially discontinuous discretizations. We then perform a systematic numerical comparison of five relevant finite element pairs used in oceanic and coastal flows. In short, the following facts are observed:

- Large physical viscosity is required to obtain optimal order of convergence for P_1^{NC}-P_1 and P_1^{DG}-P_1 pairs.
- The accuracy of Discontinuous Galerkin discretization of Coriolis dominated flows is deteriorated by the lack of control on the jumps of tangent velocity.
- P_1^{DG}-P_2 gives accurate results in all ranges of flow, at the expense of second order shape function for elevation, hence higher order quadrature rules.
- P_1^{NC}-P_1^{NC} appears to behave optimally in all ranges of flow, with a reasonable number of degrees of freedom. The diffusion terms are naturally handled by the discrete space.

In terms of CPU efficiency, sharp conclusions are difficult to draw, as these are strongly implementation dependent. For explicit computations, using the same number of elements, P_1^{NC}-P_1^{NC} and P_1^{DG}-P_1^{DG} have truly similar cost per time-step, as most of the CPU time is spent computing the finite element integrals, that require the same accuracy for both finite element pairs. The computation of spatial operators for P_1^{DG}-P_2 is more expensive as the higher order of the shape function for elevation requires more accurate quadrature rules. For

implicit computations, most of the CPU time is spent in the linear solver. The size of the system depends on the number of degree of freedom per element. The requirements of $P_1^{DG} - P_1^{DG}$ and $P_1^{DG} - P_2$ pairs are similar, with respectively 9 and 8 dof per element. $P_1^{NC} - P_1^{NC}$ behaves optimally in all our testcases, and uses only 4.5 degree of freedom per element. Therefore, it is an interesting alternative that should be further studied to confirm its promising behavior.

ACKNOWLEDGEMENTS

Richard Comblen is Research fellow with the Belgian National Fund for Scientific Research (FNRS). Jonathan Lambrechts is Research fellow with the Belgian Fund for Research in Industry and Agriculture (FRIA). The present study was carried out within the scope of the project "A second-generation model of the ocean system", which is funded by the Communauté Française de Belgique, as Actions de Recherche Concertées, under contract ARC 04/09-316.

REFERENCES

1. Mesinger F, Arakawa A. *Numerical Methods used in Atmospheric Models.* GARP Publications Series No. 17, WMO - ICSU, 1976.
2. Griffies S. *Fundamentals of ocean climate models.* Princeton University Press, 2004.
3. Hartmann R, Houston P. Adaptive discontinuous Galerkin finite element methods for the compressible Euler equations. *Journal of Computational Physics* 2002; **183**:508–532.
4. Bernard PE, Chevaugeon N, Legat V, Deleersnijder E, Remacle JF. High-order h-adaptative discontinuous Galerkin methods for ocean modelling. *Ocean Dynamics* 2007; **57**:109–121.
5. Burbeau A, Sagaut P. A dynamic p-adaptive discontinuous Galerkin method for viscous flow with shocks. *Computer and Fluids* 2005; **34**:401–417.
6. Cockburn B, Shu CW. The Runge-Kutta discontinuous galerkin method for conservation laws v - multidimensional systems. *Journal of Computational Physics* 1998; **141**:191–224.
7. Chevaugeon N, Xin J, Hu P, Li X, Cler D, Flaherty JE, Shephard MS. Discontinuous Galerkin methods applied to shock and blast problems. *Journal of Scientific Computing* 2005; **22-23**:227–243.
8. Remacle JF, Frazão SS, Li X, Shephard MS. An adaptive discretization of shallow-water equations based on discontinuous Galerkin methods. *International Journal for Numerical Methods in Fluids Volume* 2006; **52**:903–923.
9. Nair RD, Thomas SJ, Loft RD. A discontinuous Galerkin global shallow water model. *Monthly Weather Review* 2005; **133**:876–888.
10. Giraldo FX. High-order triangle-based discontinuous Galerkin methods for hyperbolic equations on a rotating sphere. *Journal of Computational Physics* 2006; **214**:447–465, doi:doi:10.1016/j.jcp.2005.09.029.
11. Aizinger V, Dawson C. A discontinuous Galerkin method for two-dimensional flow and transport in shallow water. *Advances in Water Resources* 2002; **25**:67–84.
12. Kubatko EJ, Westerink JJ, Dawson C. *hp* discontinuous galerkin methods for advection dominated problems in shallow water flows. *Computational Methods in Applied Mechanics and Engineering* 2006; **196**:437–451.
13. Bernard PE, Remacle JF, Legat V. Boundary discretization for high order discontinuous Galerkin computations of tidal flows around shallow water islands. *International Journal for Numerical Methods in Fluids* 2008; doi:10.1002/fld.1831.
14. Schwanenberg D, Harms M. Discontinuous Galerkin finite-element method for transcritical two-dimensional shallow water flows. *Journal of Hydraulic Engineering* 2004; **130**:412–421.
15. Arnold DN, Brezzi F, Cockburn B, Marini LD. Unified analysis of discontinuous Galerkin methods for elliptic problems. *SIAM journal on numerical analysis* 2002; **39**:1749–1779.
16. Cockburn B, Shu C. The local discontinuous Galerkin finite element method for convection-diffusion systems. *SIAM Journal on Numerical Analysis* 1998; **35**:2440–2463.
17. Riviere B. *Discontinuous Galerkin Methods for Solving Elliptic and Parabolic Equations: Theory and Implementation*, *Frontiers in Mathematics*, vol. 35. SIAM, 2008.
18. Donea J, Huerta A. *Finite Element Methods for Flow Problem.* Wiley, 2003.
19. Bova SW, Carey GF. An entropy variable form and applications for the two-dimensional shallow water equations. *International Journal For Numerical Methods In Fluids* 1996; **23**:29–46.

20. Hauke G. A symmetric form for computing transient shallow water flows. *Computer Methods in Applied Mechanics and Engineering* 1998; **163**:111–122.
21. Ribeiro FLB, Galeão AC, Landau L. Edge- based finite element method or shallow water equations. *International Journal For Numerical Methods In Fluids* 2001; **36**:659–685.
22. Hauke G. A stabilized finite element method for the Saint-Venant equations with application to irrigation. *International Journal For Numerical Methods In Fluids* 2002; **38**:963–984.
23. Le Roux DY, Staniforth A, Lin CA. Finite elements for shallow-water equation ocean model. *Monthly Weather Review* 1998; **126**:1931–1951.
24. Le Roux DY, Lin CA, Staniforth A. A semi-implicit semi-Lagrangian finite-element shallow-water ocean model. *Monthly Weather Review* 2000; **128**:1384–1401.
25. Le Roux DY. A new triangular finite-element with optimum constraint ratio for compressible fluids. *SIAM Journal on Scientific Computing* 2001; **23**:66–80.
26. Hanert E, Roux DYL, Legat V, Deleersnijder E. An efficient Eulerian finite element method for the shallow water equations. *Ocean Modelling* 2005; **10**:115–136.
27. Le Roux DY, Sene A, Rostand V, Hanert E. On some spurious mode issues in shallow-water models using a linear algebra approach. *Ocean Modelling* 2005; **10**:83–94.
28. Le Roux DY. Dispersion relation analysis of the $P_1^{NC} - P_1$ finite-element pair in shallow-water models. *SIAM Journal on Scientific Computing* 2005; **27**:394–414.
29. Hanert E, Walters RA, Le Roux DY, Pietrzak JD. A tale of two elements: $P_1NC - P_1$ and RT_0. *Ocean Modelling* 2008; doi:10.1016/j.ocemod.2008.07.002.
30. Hua BL, Thomasset F. A noise-free finite element scheme for the two-layer shallow water equations. *Tellus* 1984; **36A**:157–165.
31. Bernard PE, Remacle JF, Legat V. Modal analysis on unstructured meshes of the dispersion properties of the $P_1^{NC} - P_1$ pair. *Ocean Modelling* 2008; doi:10.1016/j.ocemod.2008.03.005.
32. Cotter CJ, Ham DA, Pain CC. A mixed discontinuous/continuous finite element pair for shallow-water ocean modelling. *Ocean Modelling* 2009; **26**:86–90, doi:10.1016/j.ocemod.2008.09.002.
33. Cotter CJ, Ham DA, Pain CC, Sebastian Reich S. LBB stability of a mixed Galerkin finite element pair for fluid flow simulations. *Journal of Computational Physics* 2009; **228**:336–348, doi: 10.1016/j.jcp.2008.09.014.
34. Shahbazi K. An explicit expression for the penalty parameter of the interior penalty method. *Journal of Computational Physics* 2005; **205**:401–407.
35. LeVeque RJ. *Finite Volume Methods for Hyperbolic Problems*. Cambridge Texts in Applied Mathematics, Cambridge University Press, 2002.
36. Geuzaine C, Remacle JF. Gmsh: a three-dimensional finite element mesh generator with buit-in pre- and post-processing facilities. *International Journal for Numerical Methods in Engineering* 2008 (submitted); .
37. Brezzi F, Fortin M. *Mixed and Hybrid Finite Element Methods*. No. 15 in Springer Series in Computational Mathematics, Springer-Verlag, 1991.
38. Le Roux DY, Rostand V, Pouliot B. Analysis of numerically induced oscillations in 2d finite-element shallow-water models part I: inertia-gravity waves. *SIAM Journal on Scientific Computing* 2007; **29**:331–360.
39. Le Roux DY, Rostand V, Pouliot B. Analysis of numerically induced oscillations in 2d finite-element shallow-water models part II: free planetary waves. *SIAM Journal on Scientific Computing* 2008; **30**:1971–1991.
40. Bassi F, Crivellini A, Di Pietro DA, Rebay S. An artificial compressiblility flux for the discontinuous Galerkin solution of the incompressible Navier-Stokes equations. *Journal of Computational Physics* 2006; **218**:794–815.
41. Di Pietro DA. Analysis of discontinuous Galerkin approximation of the Stokes problem based on an artificial compressibility flux. *International Journal for Numerical Methods in Fluids* 2007; **55**:793–813.
42. Cockburn B, Kanschat G, Schötzau D, Schwab C. Local discontinuous Galerkin methods for the Stokes system. *SIAM Journal on Numerical Analysis* 2002; **40**:319–343.
43. Comblen R, Legrand S, Deleersnijder E, Legat V. A finite element method for solving the shallow water equations on the sphere. *Ocean Modelling* 2008; doi:10.1016/j.ocemod.2008.05.004.